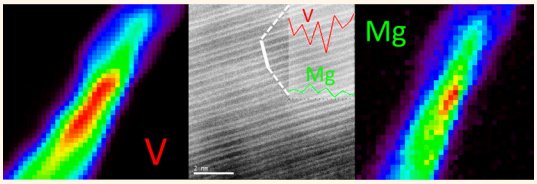
# Nanostructured Layered Cathode for Rechargeable Mg-Ion Batteries

Sanja Tepavcevic,*,† Yuzi Liu,† Dehua Zhou,‡ Barry Lai,§ Jorg Maser,§ Xiaobing Zuo,§ Henry Chan,⊥ Petr Král,⊥,∥ Christopher S. Johnson,‡ Vojislav Stamenkovic,# Nenad M. Markovic,# and Tijana Rajh*,†

†Center for Nanoscale Materials, ‡Chemical Sciences and Engineering Division, §X-ray Science Division, and #Materials Science Division, Argonne National Laboratory, 9700 S. Cass Avenue, Argonne, Illinois 60439, United States and ⊥Chemistry Department and ∥Physics Department, University of Illinois at Chicago, Chicago, Illinois 60607, United States

**ABSTRACT** Nanostructured bilayered $V_2O_5$ was electrochemically deposited within a carbon nanofoam conductive support. As-prepared electrochemically synthesized bilayered $V_2O_5$ incorporates structural water and hydroxyl groups, which effectively stabilizes the interlayers and provides coordinative preference to the $Mg^{2+}$ cation in reversible cycling. This open-framework electrode shows reversible intercalation/deintercalation of $Mg^{2+}$ ions in common electrolytes such as acetonitrile. Using a scanning transmission electron microscope we demonstrate that $Mg^{2+}$ ions can be effectively intercalated into the interlayer spacing of nanostructured $V_2O_5$, enabling electrochemical magnesiation against a Mg anode with a specific capacity of 240 mAh/g. We employ HRTEM and X-ray fluorescence (XRF) imaging to understand the role of environment in the intercalation processes. A rebuilt full cell was tested by employing a high-energy ball-milled Sn alloy anode in acetonitrile with $Mg(ClO_4)_2$ salt. XRF microscopy reveals effective insertion of Mg ions throughout the $V_2O_5$ structure during discharge and removal of Mg ions during electrode charging, in agreement with the electrode capacity. We show using XANES and XRF microscopy that reversible Mg intercalation is limited by the anode capacity.




**KEYWORDS:** nanostructured electrodes · electrochemical synthesis · bilayered $V_2O_5$ · hydrated oxide · magnesium ion battery · XRF mapping of transporting ions · HAADF

In recent years, significant attention has been devoted to the development of rechargeable batteries beyond $Li^+$-ion systems, in order to alleviate energy storage needs associated with the anticipated growth in renewable energy systems.[1] Development of batteries that implement multivalent transporting ions such as environmentally friendly (nontoxic) and highly abundant magnesium (2.9% as compared to 0.002% for Li) is an exciting opportunity because a two-electron $Mg/Mg^{2+}$ redox reaction can potentially lead to a high theoretical volumetric capacity (3832 mAh $cm^{-3}$), thus rivaling that of Li-metal batteries.[2] Contrary to lithium batteries, however, the development of Mg rechargeable systems (or any other multivalent system) did not make significant progress in the past decade due to mainly two reasons: (i) kinetically hindered intercalation and diffusion of Mg ions within cathode materials and (ii) incompatibility of high-performance electrolytes with metallic anodes and/or high-voltage cathodes.[3−5]

In 2008, Aurbach *et al.*[6] demonstrated the first viable rechargeable magnesium battery technology with an electrolyte solution based on Mg organohaloaluminate salts, a magnesium metal anode, and a $Mg_xMo_3S_4$ (Chevrel) cathode. Magnesium electrodes behave reversibly in Grignard reagent solutions in ethers (RMgX, R = alkyl, aryl groups and X = halide, Cl, Br, *etc.*) likely due to magnesium inactivity toward ethers and RMgX compounds.[7] However, despite the high reversibility of Mg electrodes in Grignard/ether solutions, organohaloaluminate/ether electrolytes exhibit a relatively narrow electrochemical stability window (up to 2.2 V *vs* Mg), thus greatly limiting the choice of cathodes for Mg batteries.[5] In order to improve Mg battery performance, new electrolyte solutions with a wide electrochemical window[8] as well as novel polymeric gel electrolytes[9] are beginning to emerge.[10] However, all currently proposed electrolytes are based on ethers, and from the viewpoints of safety, reliability, and their compatibility with both anodes and high-voltage cathodes, they are still not adequate.

* Address correspondence to T. Rajh (rajh@anl.gov); S. Tepavcevic (sanja@anl.gov).

Received for review April 23, 2015 and accepted July 14, 2015.

**Published online** July 14, 2015
10.1021/acsnano.5b02450

© 2015 American Chemical Society

The use of ionic materials for the intercalation of magnesium ions with a large charge density, however, causes a substantial polarization on the cathode. In metal oxide electrodes, intercalation of ions with a large charge density leads to relocalization of the electron density in the host material from collective orbitals onto oxygen p-orbitals. As such, the resulting polarized host electrode is not well suited to facile reversible intercalation processes. In particular, dense crystalline structures of metal oxides limit the diffusion of Mg ions. The common approach to bypass this limitation is to use materials with "soft-bonding" ion channels able to modulate polarization effects. For example, chevrel phases (CP) $M_xMo_6T_8$ (M = metal, T = S, Se)[6] in their microcrystalline state or $TiS_2$ nanotubes[11] or $MoS_2$ nanoribbons[12] allow for fast and reversible Mg insertion at ambient temperatures. However, a fundamental disadvantage is their low average voltage of ~1.1 V *vs* $Mg/Mg^{2+}$. On the other hand, polyanion framework electrode materials, such as strongly bonded $Mg_{1.03}Mn_{0.97}SiO_4$, have a high redox voltage, but they suffer from sluggish Mg diffusion kinetics, caused by both strong electrostatic interactions and low electronic conductivity, resulting in poor charge- and discharge-rate capability.[13]

Among various cathode materials considered for Mg-ion batteries, vanadium-based oxides have been intensively studied for many decades, due to the availability of multiple valence states ($V^{5+} \rightarrow V^{3+}$), offering the potential for high energy density associated with multiple electron transfer.[14] The usual solid-state synthesis of vanadium pentoxide ($V_2O_5$) *via* the hydrothermal heating of aqueous solutions leads to the well-known orthorhombic $V_2O_5$. Many other structures based on vanadium oxide have been described in the literature, having different types of vanadium coordination polyhedra.[2] Previous electrochemical studies included $V_2O_5$/carbon composites,[15] thin-film $V_2O_5$ electrodes,[16] $VO_x$ nanotubes,[17] and Mg intercalated vanadium oxides $Mg_xV_2O_5$,[18] albeit with fading capacities upon prolonged cycling.

In this work, we have used electrochemical synthesis, which allows formation of unique nanostructured bilayered $V_2O_5$ structure with wide and adjustable interlayer spacing. This method also provided effective incorporation of defects, water, and hydroxyl groups, which, in turn, fostered electron transfer and (de)-intercalation of highly charged $Mg^{2+}$ ions. We hypothesize that the presence of adsorbed and hydrogen-bonded water is important for a double-layer capacitance behavior, while the presence of structural hydroxyl groups is critical for the intercalation processes.

We demonstrated that electrochemically synthesized nanostructured $V_2O_5$ can effectively intercalate Mg ions between its bilayers and can be discharged against a Mg anode to create a fully loaded Mg-containing cathode in the discharged state (240 mAh/g). We employed HRTEM and X-ray fluorescence (XRF) imaging to understand the role of environment in the Mg-ion intercalation processes. Classical molecular dynamics simulations were used to understand the structure of a Mg-intercalated $V_2O_5$ cathode. This cathode was successfully coupled in a rebuilt full cell with a high-energy ball-milled Sn/C composite anode in high-voltage/conductivity electrolytes, such as acetonitrile with $Mg(ClO_4)_2$ salt, to reach a considerable reversible capacity that improves with cycling at elevated voltages. We have also shown, using X-ray absorption near-edge structure (XANES) and XRF, that reversible Mg intercalation is limited by the anode capacity.

## RESULTS AND DISCUSSON

**Electrochemical Preparation of Nanostructured $V_2O_5$ Electrodes.** One of the main issues in the application of nanostructured materials for energy storage is the integration of nanoscale materials into mesoscale hierarchical architectures used in real devices. Electrochemical synthesis intrinsically results in nanoscale architectures electronically coupled to conductive supports, allowing their integration with other battery components, without the need for further post-treatments before utilization.[19] The electrons that drive electrochemical synthesis create reactive species that propagate chemical reactions fostering electrical connectivity to the extent that electrons can penetrate the structure. Therefore, electrodes grown by an electrochemical synthesis naturally evolve toward an optimized structure, which can achieve a high power, energy density, and stability, needed in the next generation of hybrid systems. On the other hand, an electronically interconnected nanoporosity allows short diffusion lengths of transporting ions and a full participation of the whole cathode in achieving its theoretical capacity.

In our earlier work,[19] we synthesized nanostructured $V_2O_5$ by electrodeposition from vanadyl sulfate on a Ni substrate and obtained a thin film of nanostructured $V_2O_5$. Herein, we developed a new procedure for electrodepositing bilayered $V_2O_5$ within a highly conductive commercially available substrate: carbon nanofoam (CNF). Figure 1 shows an HRTEM image of an "as-prepared" individual $V_2O_5$ nanoribbon in conjunction with a SEM image of an interconnected network of nanoribbons within a CNF framework (inset, Figure 1). Because of the electronic conduction and high porosity of CNF, it is possible to increase the mass loading of an active material up to 30 mg/cm$^2$, without any mechanical problems. This easy bulk electrodeposition method allows straightforward scaling up of electrodes for a large-scale production. Importantly, this synthetic approach provides an intimate direct contact of bilayered $V_2O_5$ with the carbon support, without the addition of binders or conductive

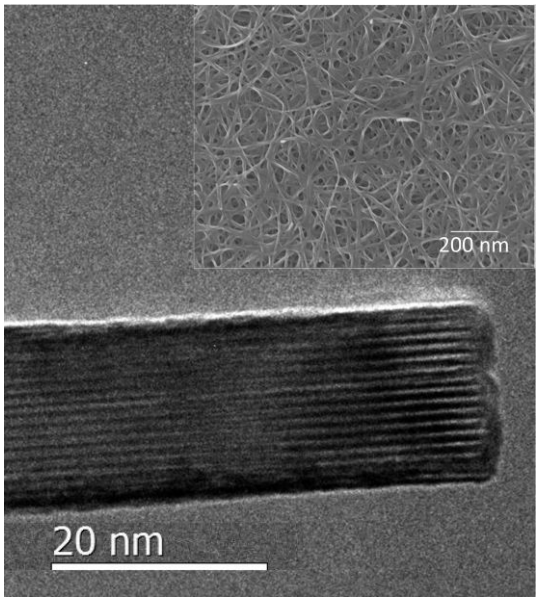



**Figure 1. HRTEM image of a nanoribon of bilayered $V_2O_5$ electrochemically grown on a carbon nanofoam (CNF) substrate. Inset shows a SEM image of interconnected nanoribon architecture electrochemically grown on CNF.**

high surface area carbon diluents. The electrochemical synthesis within a conductive CNF developed in this work provides an exceptionally large interlayer distance of 13.5 Å of $V_2O_5$, compared to $d$ = 8.8−11 Å[19] obtained by other methods. This large interlayer distance was found to be crucial for an efficient cycling of large Na ions, due to balancing electrostatic forces present during cycling. We hypothesize that the large spacing and structural adaptability of $V_2O_5$ might lead to reversible cycling of small but polarizing Mg ions, as both the dipole moment interaction $\propto R^{-2}$ and the polarizability component $\propto R^{-4}$ that constitute material polarization rapidly decay within the large interspace distance between the $V_2O_5$ layers.[20]

**$Mg^{2+}$ Enrichment.** Electrochemical synthesis facilitates also Mg enrichment of as-prepared $V_2O_5$. Bilayered $V_2O_5$ electrodes are originally synthesized in the charged state; in order to operate effectively in the Mg-ion full cell, it is necessary to introduce the source of magnesium into the cathode. An electrochemical preconditioning approach was used to incorporate Mg ions in the cathode: $V_2O_5$ half-cells were discharged galvanostatically at 20 $\mu$A to the potential 0.2 V *versus* $Mg/Mg^{2+}$. The first galvanostatic discharge voltage profile of the Mg half-cell (with polished Mg foil as an anode) is shown in the inset of Figure 2. The voltage starts out at an OCV of ∼1.7 V and then progressively is driven to a lower cutoff potential of 0.2 V *vs* the $Mg/Mg^{2+}$ anode. The specific capacity of 240 mAh/g was obtained in this preconditioning procedure, suggesting reduction of vanadium to $V^{4+}$. This oxidation state was also confirmed by direct measurements of the V oxidation state using X-ray absorption

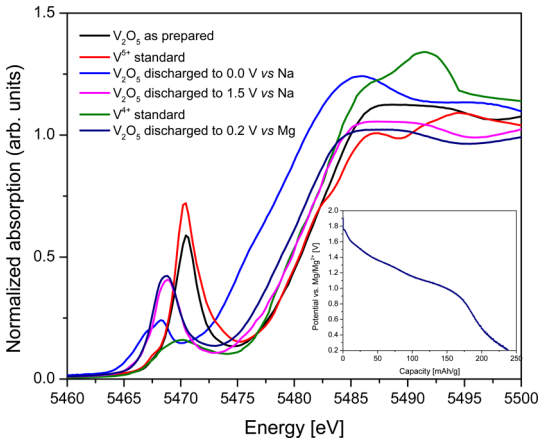



**Figure 2. Half cells: Normalized V K-edge XANES for as-prepared, bilayered $V_2O_5$ ($V^{5+}$), $V_2O_5$ after Mg enrichment ($V^{4+}$), $V_2O_5$ after Na enrichment ($V^{4+}$ and $V^{3+}$), and two standards ($V^{5+}$ and $V^{4+}$). Inset: Chronopotentiometric curves of Mg insertion into nanostructured $V_2O_5$ in 1 M $Mg(ClO_4)_2$/AN.**

spectroscopy (XAS),[21] as the main edge position of the discharged sample was close to that of $VO_2$ ($V^{4+}$ oxidation state standard). It should be mentioned that this oxidation state also suggests $MgV_2O_5$ stoichiometry (one Mg per $V_2O_5$ molecule). Furthermore, the intensity of the V K-edge pre-edge peak, related to the probability of the forbidden s → d dipole electronic transition of vanadium, decreases with the insertion of Mg ions during preconditioning. The lower intensity of this peak reflects the formation of a centrosymmetric octahedral symmetry of vanadium sites, suggesting the ordering of a local vanadium environment upon insertion of Mg.

The distribution of Mg transporting ions within $V_2O_5$ was furtherer investigated using XRF microscopy. The importance of direct imaging of the distribution of transporting ions in conjunction with elemental mapping of the electrode material is that element colocalization studies directly report the mechanism of charge compensation. Transporting ions such as $Li^+$ or $Na^+$ have too low fluorescence yields and efficiencies for detection; however, $Mg^{2+}$ ions are more readily mapped within the matrix of the host $V_2O_5$. Figure 3 shows a fluorescence image of Mg and V, in a Mg-enriched rod-like particle extracted from CNF. The linear color scale ranges from black (low intensity) to red (high intensity). The resulting fluorescence intensity map provides information on the total Mg content in the volume illuminated by the beam at each scanning step. The images show that distributions of both Mg and V mostly follow intensities expected for a rod-like object: intensities peaked in the middle, where the sample was thickest, and decreased toward the edges, where the sample was thinnest (the thickness of the sample is shown by X-ray transmittance, Figure S1), suggesting that both transporting ions (Mg) and host elements (V) are colocalized throughout the structure, confirming intercalation of Mg within the $V_2O_5$ sample.

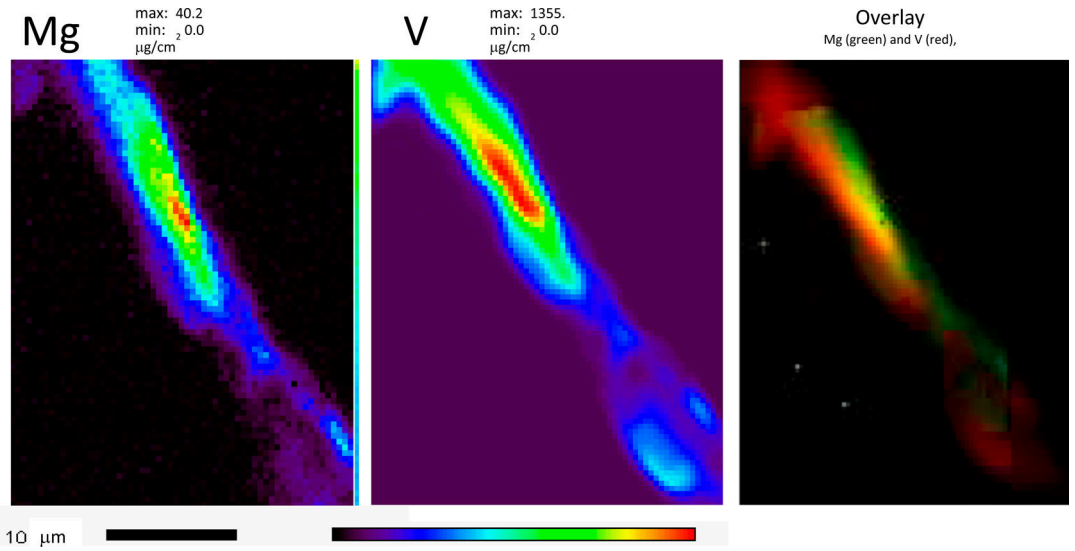



**Figure 3. XRF maps of Mg (a) and V (b) in a Mg-enriched sample discharged at 0.02 V *vs* the Mg anode obtained using 5.45 nd 10.1 keV X-rays, respectively. The images were derived from detectors placed on the right with a 15-degree takeoff. Black pixels represent the lowest fluorescence intensity, while red pixels correspond to the highest. (c) Overlay of the Mg and V maps shows the effect of self-absorption of Mg fluorescence.**

While imaging of the Mg distribution provides direct information about the distribution of Mg after insertion within the sample, the quantitative interpretation of the results needs further considerations. Mg is a light element, with a low energy of ionization, and emits low-energy X-ray fluorescence. As a consequence, the fluorescence radiation of Mg experiences strong self-absorption characteristic for imaging of all light elements due to nonspecific absorption of low-energy X-rays through the sample.[22] In our measurements the detector was positioned at a 15-degree takeoff angle (right), and the intensity from the opposite (left) side of the rod was reduced due to enhanced self-absorption associated with larger path lengths through the sample (Figure 3A). However, in contrast to Mg, the V X-ray fluorescence is not nearly as affected by self-absorption due to higher energy X-ray fluorescence, and the V image in Figure 3B is more consistent across the sample. The overlay of the intensity map of Mg (green) and V (red) in Figure 3C reflects the signal detection inhomogeneity arising from Mg fluorescence self-absorption. By carefully modeling the absorption of low-energy Mg emission through a $VO_2$ rod (SI, Figure S2 and Table S1), one obtains an absorption correction factor and Mg/V ratio based on the experimental geometry. The corrected molar ratio reveals a molecular formula of $Mg_{0.7}V_2O_5$, suggesting an oxidation state of V close to +4.3. This value is in very good agreement with sample average measurements of the $V^{+4}$ oxidation state obtained using XANES (Figure 2) and reflects some distribution of the oxidation states at different parts of the $V_2O_5$ electrode.

**$Mg^{2+}$-Ion Charge, Role of Water, and Solvent Co-intercalation.** Relatively slow transport of $Mg^{2+}$ ions in common hosts was shown to be related to their divalent character. Electrochemically synthesized nanostructured $V_2O_5$ has a very unique morphology and structure compared to similar structures created by sol−gel methods.[23] Unique to electrochemical preparation is formation of a highly hydrated sample (Figure S3), with an exceptionally wide interlayer spacing of 13.5 Å due to incorporation of structural water between the layers. Novak and Desilvestro[24] studied electrochemical intercalation of $Mg^{2+}$ into conventional orthorhombic $V_2O_5$ electrodes in an electrochemical cell using an electrolyte composed of 1 M $Mg(ClO_4)_2/CH_3CN$ (AN) with water added to AN. Using cycling voltammetry the authors found that intercalation of Mg ions coupled to reduction of $V_2O_5$ improved with the addition of water to the electrolyte. They speculated that water molecules co-intercalate with the $Mg^{2+}$ cations and provide a smaller solvation shell than the organic solvent molecules. They have also shown that reduction of $V_2O_5$ corresponding to capacities of ~170 mAh/g could be achieved; however, the capacity drastically decayed upon further cycling. The authors have shown that added water, essential for reversible intercalation of $Mg^{2+}$, is removed during the cycling and released back to the electrolyte, resulting in the decay of electrode capacity.[25]

Electrochemical synthesis of bilayered $V_2O_5$ results, however, in incorporation of three types of water: (1) mostly free water reversibly adsorbed between the $V_2O_5$ layers; (2) bonded water incorporated into the layers cross-linked through hydrogen bonds; and (3) structural hydroxyl groups typical for electrochemically synthesized oxides.[26] We have shown using thermogravimetric analysis that bound water (reversibly absorbed and hydrogen-bonded water) is removed upon annealing of as-prepared samples at 120 °C under vacuum (Figure S3). Removal of weakly bound water

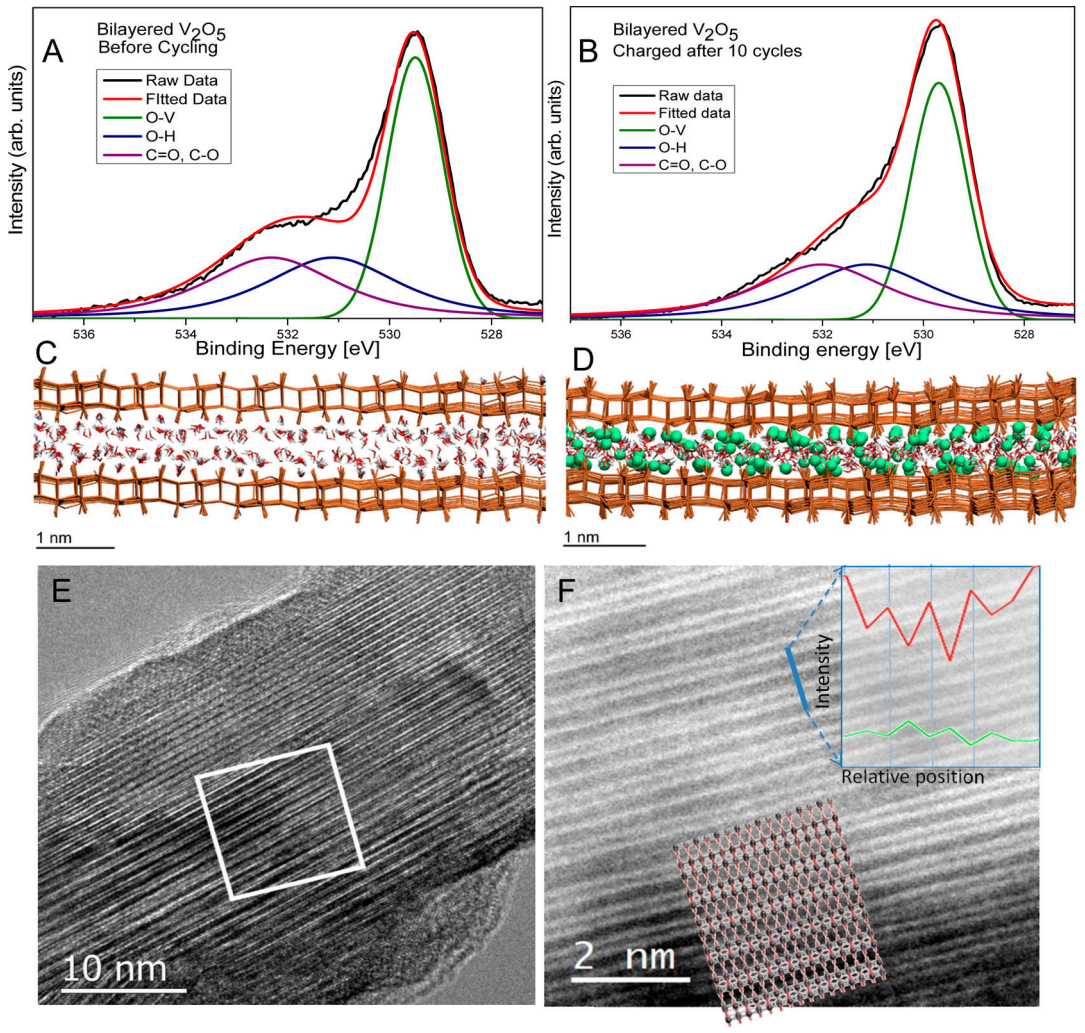



**Figure 4. XPS spectra of bilayered $V_2O_5$ before (A) and after 10 cycles of charging with $Mg^{2+}$ ions (B) in the O 1s core level region in conjunction with molecular dynamics simulation of the $V_2O_5$ bilayer immersed in water (C) and in the presence of Mg ions with V in the +4 state in the presence of water (D). HRTEM image of Mg-enriched $V_2O_5$ (E) in conjunction with an HAADF image (F), in which the relative position of V and Mg atoms obtained with EDS is shown in the inset (V: red, Mg: green). The lattice model in the viewing direction [102] is also shown on the HAADF image, in which bright lines depict the V plane.**

only mildly alters the structure with contraction of the interlayer spacing to a distance of 12 Å,[27] while structural hydroxyl groups[28] still remain in the structure (Figure 4A) with a stoichiometry of $V_2O_5 \cdot 0.6H_2O$.[29] The structure becomes significantly altered, however, after removal of structural hydroxyl groups (achieved only upon annealing above 300 °C), when the bilayered structure collapses into crystalline orthorhombic $V_2O_5$ with poor electrochemical performance.

We have used computational methods to simulate $V_2O_5$ bilayered structures with different contents of water and obtained that the spacing between bilayers corresponds to the spacing observed in X-ray diffraction measurements (Figure S4) and HRTEM images (Figure 1). The amount of water that swells $V_2O_5$ to observed interlayer spacing was found to correspond to ~2 mol of $H_2O$ per mol of $V_2O_5$ and was confirmed by thermogravimetric analysis. We believe that this large amount of water can facilitate the intercalation of Mg ions. It has been shown previously that solvation of Mg ions with water is energetically favorable in a mixed solvent. It was found that water molecules substitute acetonitrile in the first solvation shell in a linear fashion with up to six water molecules per Mg ion.[30] Although preferentially coordinated with six molecules of water, the energies of water solvation quickly decrease with increasing water content, forming a stable configuration with four water molecules in the first solvation shell.[31] Due to the preferential solvation of the $Mg^{2+}$ by water compared to acetonitrile and greater affinity of acetonitrile to water already coordinated to $Mg^{2+}$, the reversible co-intercalation of already hydrated Mg ions can be expected.[30] A water solvation shell partially shields the charge of the $Mg^{2+}$ cations, decreasing polarization effects and the strength of their interaction with apical oxygens and hydroxyl groups. Indeed, unlike added and weakly bound water, strongly bound structural hydroxyl groups remain in the structure

during cycling (Figure 4B) and act as a lubricant for reversible (de)intercalation of solvated $Mg^{2+}$ ions between enlarged galleries of electrochemically synthesized $V_2O_5$. In contrast to water added to electrolyte that can enter and swell $V_2O_5$ but easily comes out of the structure upon cycling due to its weak interaction with the metal oxide framework,[24,25] structural hydroxyl groups are covalently linked to $V_2O_5$ and therefore do not get depleted during cycling. On the contrary, strongly bound hydroxyl groups can participate in hydrogen bonding of water molecules that hydrate $Mg^{2+}$ ions, facilitating intercalation of integrated solvated $Mg^{2+}$. Thus, the interaction of hydrated $Mg^{2+}$ with $V_2O_5$ will depend on the relative ratio between the energies for further solvation of hydrated $Mg^{2+}$ with acetonitrile and the energy of interaction with structural hydroxyl groups in a bilayered $V_2O_5$ structure, and this ratio will determine the ability for reversible $Mg^{2+}$ ion intercalation.

Similar reasoning can also account for previously shown behavior of microcrystalline $V_2O_5$, where addition of water to the electrolyte solution improved insertion (albeit limited) of Mg ion.[4] Indeed, we find using molecular dynamics (MD) simulation of a $V_2O_5$ model slab composed of three bilayers immersed in water that water swells to a structure with an interlayer spacing of ~12 Å by taking up water to screen all exposed surfaces, reaching two layers of water per $V_2O_5$ slab (Figure 4C). MD simulations suggest that upon insertion of Mg ions into the $V_2O_5$ structure, the spacing between bilayers narrows to ~11 Å due to the interaction of Mg ions with bilayer apical oxygens and structural hydroxyl groups (Figure 4D). Although the spacing decreases, MD simulations show that a significant amount of water remains in the structure, solvating inserted Mg ions. Figure 4E presents the HRTEM image of the well-crystallized area showing the lattice fringes of the layered $V_2O_5$ structure after Mg ions were intercalated in the structure featuring a spacing of 6.0 to 6.4 Å. It can be seen from the image that the bilayer distance is not uniform across the whole imaged area, which is consistent with the broad peak observed in the XRD measurements corresponding to the interlayer spacing. On close inspection of the fringes by using a high-angle annular dark field (HAADF) image using scanning transmission microscopy (STEM) (Figure 4F) of the selective area (marked in Figure 4C with a white square) one can see that each of the widely spaced fringes is actually composed of two closely spaced bright lines of V planes with a spacing of 1.87 Å and two V planes separated by 3.40 Å. These spacings are consistent with the structure proposed by MD simulations shown in a viewing direction of [1 0 2] (Figure 4F), which depicts also a lattice model of monoclinic bilayered base-facing square-pyramidal $V_2O_5$ with lattice parameters $a$ = 11.65 Å, $b$ = 3.62 Å, and $c$ = 11 Å with $\beta$ = 88.63°. The signal intensity of V and Mg from an EDX line scan along the blue line in the HAADF image is shown as the inset. We can see that the higher Mg intensity appears in conjunction with the lower V intensity and *vice versa*. This indicates that the Mg ions are inserted in between the V layers. The overall lower intensity of Mg compared to V is again the consequence of self-absorption of low-energy X-rays emitted by Mg in a low takeoff angle in which the detector is configured in the microscope.

Our MD simulations suggest that Mg ions are placed close to the oxygen atoms that terminate bilayers (Figure 4D). The insertion of Mg ions in the $V_2O_5$ bilayer structure does not cause removal of the first coordination water shell that solvates the ions. Although accompanied by closing of the gap between the bilayers, intercalation does not result in the collapse of the bilayered structure. Upon intercalation, some of the coordination sites of the Mg ions are replaced with an interaction with terminal hydroxyl groups from the bilayer. The interlayer water plays two important roles: it maintains a sufficient interlayered space to allow the physical diffusion of solvated Mg cations (effective size of the Mg ion with the first shell water solvent is at least 6 Å)[32] and assists in stabilizing intercalated $Mg^{2+}$ through dipole interactions. Removal of excess water reduces these two functions and results in poor electrochemical performance of highly crystalline orthorhombic $V_2O_5$.

XRD and WAXS studies show that the vanadium atomic environment within the bilayer is not significantly altered by the Mg insertion. Figure 5 shows small-angle (SAXS) and wide-angle X-ray scattering (WAXS) of $V_2O_5$ before and during cycling in the *d*-spacing range from 20 to 9 and 6 to 1 Å, respectively. The spectrum in the SAXS region confirms MD simulations and the decrease of the interlayer spacing from 13.1 Å to 11.0 Å upon intercalation of Mg ions. While diffraction features in the WAXS range show that the intralayer structure experiences changes of a tenth of an angstrom, close inspection of the range 3.5−6 Å shows more significant changes with Mg insertion. The diffraction peak at 4.7 Å disappears upon Mg insertion in conjunction with the sharpening of the feature at 3.96 Å. Modeling of X-ray diffraction using a monoclinic bilayered $V_2O_5$ structure indicates that these changes are consistent with contraction of interlayer spacing and colocalization of Mg ions near terminal hydroxyl groups. Insertion of Mg ions in the center of the interlayer gap would result in the enhancement of a diffraction peak representing half of the interlayer distance (5.9 Å [002]) and this peak would become the most intense feature in the spectrum (as observed previously by intercalation of Na ions that were placed in the middle of the interlayer gap[19]). In the discharged Mg $V_2O_5$ sample, however, the [002] diffraction peak has a smaller intensity than [202], and both of these features have a smaller intensity than the peak at 3.48 Å ([110]), which is the most intense peak

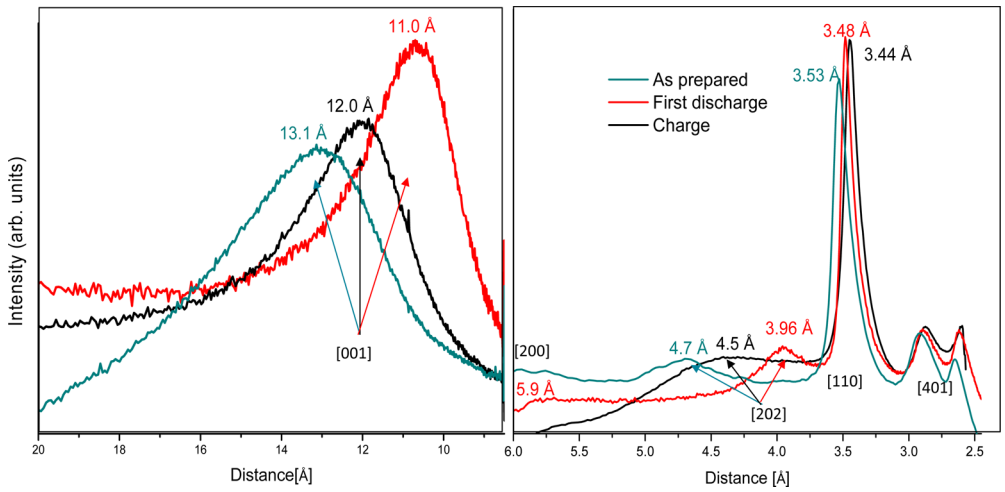



**Figure 5. SAXS and WAXS spectra of "as-prepared" (emerald) sample, Mg-enriched sample obtained by first discharge *vs* magnesium foil (red), and Mg-depleted sample (black) in conjunction with corresponding structures obtained by molecular dynamics simulations. The annotation of the scattering peaks was performed using diffraction spectra simulations using corresponding structures.**

in the spectrum, suggesting localization of Mg ions near terminal hydroxyl groups.

The *a* and *b* lattice parameters of the unit cell, which determine the intralayer dimensions, do not change significantly upon insertion, and all the bond lengths within the bilayer structure remain the same. The only parameter that is changed is the interlayer spacing, as defined by the lattice parameter *c*, which decreases upon intercalation of $Mg^{2+}$ most probably due to the strong interaction of the small doubly charged Mg ions and terminal hydroxyl groups. Observed changes are very different from the behavior found for intercalation of large Na atoms, where the size of the crystalline unit cell and the bond lengths were enlarged in order to accommodate for the intercalation of a large Na ion.[19]

**Full Mg Cells.** Identification of a suitable negative electrode for cycling of magnesium is a critical issue for the future development of magnesium ion energy storage devices. It has been shown that a Mg anode does not show good stability and reversibility due to the formation of a nonionically conductive solid electrolyte interphase. For example, in the coin cell composed of $V_2O_5$ grown on CNF (~10 mg of $V_2O_5$) and Mg foil in 1 M $Mg(ClO_4)_2/CH_3CN$ electrolyte, Mg ions cannot be redeposited on the Mg anode after the first discharge, preventing further cycling (Figure S5). When the Mg anode is, instead, replaced with graphite, Mg ions could effectively be inserted into the graphite anode but only irreversibly: they could not be removed in the following discharge step. When CNF (a hard carbon disordered material) was used as the anode itself, a reversible cycling of the full Mg cell was achieved (Figure 6A, green curve). Although the capacity of the cell was low, it was consistent with the limiting capacity of the CNF anode. Significant improvements of the battery capacity were obtained when the anode was changed to pressed nanocrystalline Sn: charge storage was increased by 10 times. This clearly shows that the capacity of the full cell in this case was strictly limited by the anode capacity. Previously it has been also shown that Sn readily forms alloys with metallic Mg, and these alloys are used for many applications ranging from lead-free soldering to anodes in lithium ion batteries.[33,34] Formation of chemical complexes such as $Mg_2Sn$ have been found to exist in the Mg−Sn melts, but the bonding was found to be only weakly interacting.[35] In this work we used nanocrystalline Sn obtained by high-energy ball-milling of bulk metallic tin.[36] Using Sn as an anode we demonstrated reversible charging of Mg-ion full cells in common electrolytes such as acetonitrile and achieved a reversible capacity of 150 mAh/g at C/15 rate. Our cycling voltammetry study (Figure 6B) of nanostructured $V_2O_5$ showed pronounced peaks in volumetric sweeps indicating reversible Faradaic reaction, while the featureless, rectangular shape for the CNF curve confirmed the capacitive origin of the CNF signal. Increasing the cycling rate to C/8 initially decreases the capacity to 100 mAh/g. Upon extended cycling, however, we observe self-improving of the electrode specific capacity previously observed in nanocrystalline systems (Figure 6C and E, 50 cycles). Figure 6D shows the corresponding d*Q*/d*V* plot of the third charge and discharge process with two distinctive and highly reversible main peaks in the range 0.0−2.0 V; one is located at about 0.95 V, and the other is located at about 1.25 V. Two peaks observed in the differential capacity curve are indicating that there are two available sites for Mg occupancy at these voltages, and their height is proportional to their availability. Furthermore, we demonstrated single-phase solid-state intercalation with the $V_2O_5$ cathode in a wide concentration range of the $Mg^{2+}$ ions (Figure 7A).

The pre-edge structure in the XANES spectrum obtained during cycling shows that upon first insertion

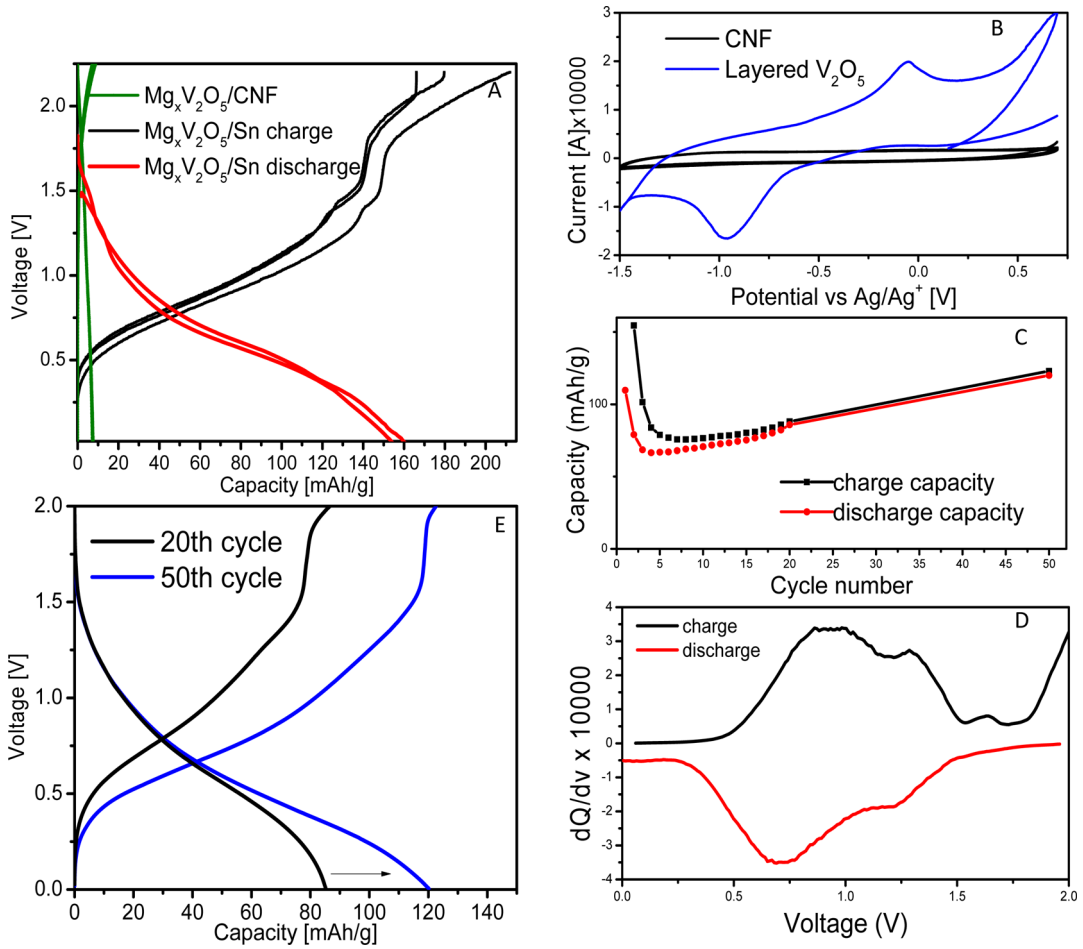



**Figure 6. Bilayered $V_2O_5$ cathode electrochemical performance. (A) First three charge−discharge cycles of Mg-enriched bilayered $V_2O_5$ *vs* nanocrystalline Sn electrode. Charge−discharge curve of the same cathode *vs* CNF is shown in green for comparison. Both cells were cycled at 20 mA/g, at C/15 rate, within the potential window of 2.2−0.0 V (*vs* $Mg/Mg^{2+}$) from 1 M $Mg(ClO_4)_2$ in acetonitrile. (B) Cyclic voltammetry of bilayered $V_2O_5$ grown on CNF (blue) and CNF in 1 M $Mg(ClO_4)_2$ in acetonitrile at 0.02 mC/s scaning rate. (C) Electrode stability measured for 50 cycles. (D) Charge−discharge curves of the same cathode cycled at the C/10 rate shown at the 20th and 50th cycles. Inset shows electrode stability study. Bottom right: corresponding differential capacity (d*Q*/d*V*) plot for the $V_2O_5$/Sn full cell. (E) Charge−discharge curves of the 20th and 50th cycle. Note the increase in the capacity in the 50th cycle.**

of Mg into the bilayered $V_2O_5$ structure, the presence of Mg ions causes ordering of bilayers that is reflected by a decrease in the intensity of the Mg pre-edge (Figure 7B). Selected area electron diffraction (SAED) images also confirm ordering in the presence of Mg ions (discharged state) where the whole grain shows polycrystalline morphology, in contrast to the charged sample, where in the absence of Mg only a few scattered larger size crystallites were observed at the edges of the sample (Figure 7C, left and center). Elemental analysis using the TEM EDAX detector shows that an approximately 10 times larger concentration of Mg ions is in the discharged sample compared to that in the charged one (Figure 7C, right). It is worth mentioning that no chlorine atoms were detected in the elemental composition of the discharged (and charged) sample, confirming that the presence of Mg in the $V_2O_5$ compound was due to the charge compensation of the reduced $V^{4+}$ ion, rather than the residual $Mg(ClO_4)_2$ salt used in the electrolyte. The position of the main edge in the XANES spectrum shows the average valence state upon repeated discharge and charge of the sample from the +4 to the +4.8 oxidation state, respectively. These results suggest either that the capacity was limited by the capacity of the Sn anode or that some of the Mg ions were retained in the structure upon repeated cycling (10 cycles). The latter case would not be necessarily surprising given that polarizing Mg ions could be retained in a highly polarized $V_2O_5$ environment, requiring still significant activation energy in order to be removed from the structure.

X-ray fluorescence microscopy studies also support reversible Mg ion intercalation with respect to V charge compensation. Figure 8 shows the change of the relative concentration between Mg and V upon cycling. While in the initial Mg-enriched discharged sample the concentration of Mg *vs* V reaches 1:3, the concentration of Mg subsequently decreases upon charging. The relative concentration of Mg *vs* V after deintercalation (during charging) was found to be 1:8,

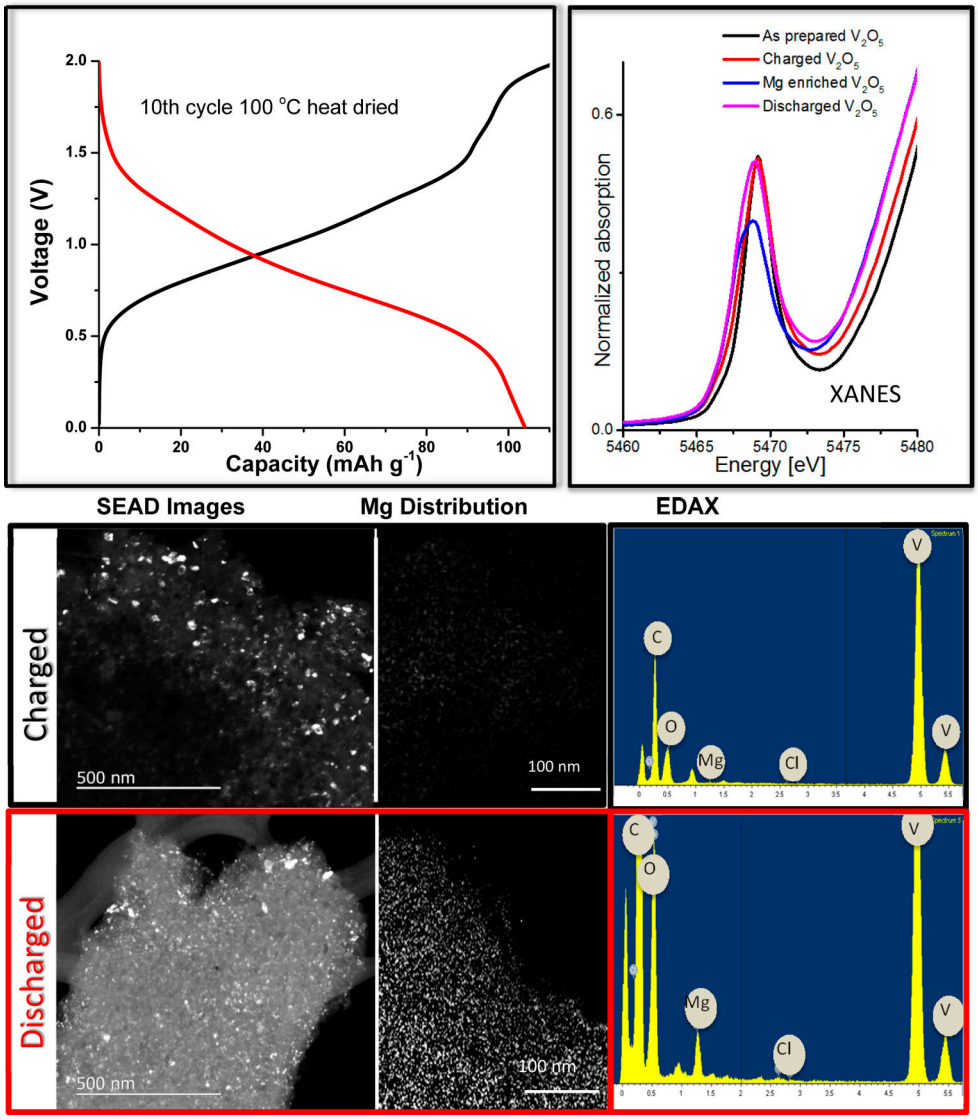



**Figure 7. (a) Charge−discharge profile of Mg-enriched bilayered $V_2O_5$ *vs* nanocrystalline Sn anode after the 10th cycle, cycled at 20 mA/g, within the potential window of 2.0−0.0 V (*vs* $Mg/Mg^{2+}$) from 1 M $Mg(ClO_4)_2$ in acetonitrile. (b) Normalized V K-edge XANES for as-prepared, Mg-enriched, and charged/discharged (after the 10th cycle) bilayered $V_2O_5$ in a full cell with a Sn anode. (c) Selected area electron diffraction and magnesium distribution during different states of charging in conjunction with elemental analysis obtained using an EDAX detector in TEM.**

suggesting a stoichiometry of $Mg_{0.25}V_2O_5$ (Figure 8 and Figure S3, Table S2). This stoichiometry is in good agreement with the determined average oxidation state of +4.8 obtained in our *in situ* XANES measurements. Although in very small concentrations, it seems that the map of Mg in the charged sample does not follow the distribution of V or the sample thickness map; rather it shows diminished fluorescence intensity from top-protruding facets, suggesting a lower diffusion energy barrier for ions inserted in exposed terraces. We also show using XRF microscopy that when nanocrystalline Sn is used as the anode, a relatively large concentration of Sn ions is transferred to the cathode area during cycling. While particles from the $V_2O_5$ cathode cycled against Mg foil (1 cycle) did not contain any impurities, the same particles cycled for 10 cycles against nanocrystalline Sn contained up to 100 $\mu g/cm^2$ of Sn and Cu in their surface layers (Figure 8, right panel). Both Sn and Cu are elements that are used in making the anode sample, Sn is used as an active anode material, and Cu is used as the electrode support, suggesting dissolution of the Sn anode in the acetonitrile electrolyte during discharging of the battery. These large ions, however, do not intercalate into the structure but concentrate at the nanoparticle interface, possibly contributing to the capacitance behavior of the electrode.

## CONCLUSIONS

In summary, we have shown efficient reversible cycling of Mg rechargeable batteries in a common electrolyte, acetonitrile, by using a nanosized open-frame

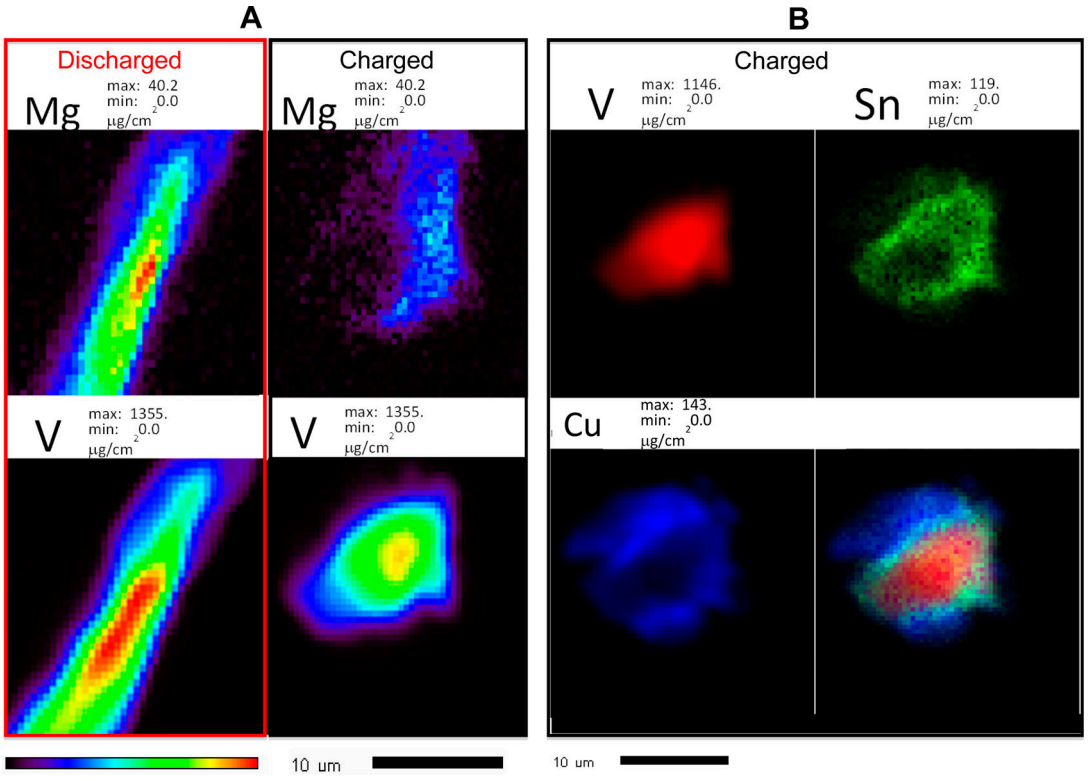



**Figure 8. (a) XRF maps of (left) Mg and V in a discharged sample and (right) charged sample obtained using 5.45 keV (top) and 10.1 keV X-rays (bottom), respectively. The images were derived from detectors placed on the right with a 15-degree takeoff. Black pixels represent the lowest fluorescence intensity, while red pixels correspond to the highest fluorescence. (b) XRF images of elemental distribution of V (top left), Sn (top right), and Cu (bottom left) and their overlay (bottom right) obtained using 10.1 keV X-rays.**

conformable $V_2O_5$ cathode paired with a Mg alloy forming a nanocrystalline tin anode. Nanocrystalline $V_2O_5$ electrochemically deposited within a porous carbon nanofoam substrate enables incorporation of structural hydroxyl groups and adsorbed water. While the CNF matrix enabled superior conductivity without any binders or conductive additives, we believe strongly bound hydroxyl groups play two important roles in reversible cycling: (i) they maintain a sufficient interlayered space to allow diffusion of Mg cations, and (ii) they reduce the symmetry of the $V_2O_5$ that contributes to the electron transfer and the magnesium intercalation. We have shown using MD simulations that the presence of structural water and ensuing hydration of Mg ions is necessary for reversible cycling of Mg ions. In response to Mg intercalation during the first Mg enrichment, the host, hydrated bilayered $V_2O_5$, compresses and orders along the *c* axes. Upon prolonged cycling (10−50 cycles) with Mg ions, the host structure becomes more disordered and polycrystalline but improves capacity for $Mg^{2+}$.

Taking advantage of the ability of X-rays to monitor both the oxidation state of electroactive vanadium atoms (XAS) and distribution of chemical species (XRF), we were able to correlate introduced charge with the distribution of transporting ions and determine the mechanism of charge compensation in Mg rechargeable systems. By employing *in situ* XANES we show that the oxidation state of V changes reversibly and cycles between an average +4.0 and +4.8 oxidation states. XRF microscopy, on the other hand, shows that Mg ions are distributed throughout the cathode in a discharged state in a near-stoichiometric ratio. Atomic precision of the elemental distribution using HAADF confirms that Mg is uniformly intercalated between two V-containing bilayers. This first demonstration of direct mapping of transporting ions within the host lattice revealed successful intercalation of Mg ions throughout the cathode in a discharged state, while only traces of Mg are detected in the charged cathode, as reversible Mg intercalation is limited by the Sn anode capacity.

## METHODS

**Synthesis of Nanostructured $V_2O_5$ Electrodes.** Nanostructured $V_2O_5$ was synthesized by electrochemical deposition on commercially available carbon nano foam (Marcketech International, Inc.). The electrochemical deposition was carried out in a two-electrode cell with CNF as the working electrode and Pt mesh as both a counter and reference electrode in aqueous 0.1 M $VOSO_4$ solution at a constant potential of 1.5 V. As-prepared bilayered

$V_2O_5$ electrodes were synthesized by vacuum annealing at 120 °C for 20 h. The crystallized orthorhombic $V_2O_5$ electrodes were obtained by annealing of as-prepared $V_2O_5$ under an $O_2$ atmosphere at 500 °C for 4 h.

**Electrochemical Insertion/Extraction of $Mg^{2+}$ and Characterization.** Magnesium half-cells were assembled in a He-filled dry glovebox into coin-type cells with a Mg foil as the negative electrode, an electrolyte of 1 M $Mg(ClO_4)_2$ (Aldrich) in acetonitrile (ACN), and a glassy fiber separator. In order to cycle, a full cell source of Mg in the system is necessary. We first discharged the $V_2O_5$ cathode to 0 V *vs* Mg foil and then opened that cell in a glovebox under an inert atmosphere. Finally we reassembled this Mg-enriched $Mg_xV_2O_5$ cathode with a Sn anode into the full cell. Full Mg cells were assembled in coin-type cells (Hohsen 2032) with a magnesium-enriched $M_xV_2O_5$ nanoribbon as the positive electrode and high-energy ball-milled Sn as the negative electrode, a glass fiber separator (Whatman GF/F), and 1 M $Mg(ClO_4)_2$/ACN as electrolyte. The traditional Sn anode was made by mixing 84 wt % active material (Sn powder, Aldrich), 4 wt % graphite (Timcal, SFG-6), 8 wt % poly- (vinylfifluoride) binder (Kynar), and 4 wt % carbon black (Toka) and pressed on Cu foil. Full Mg cells were cycled galvanostatically at varying currents between 2.3 and 0 V *vs* $Mg/Mg^{2+}$, respectively, using an automated Maccor battery tester at ambient temperature. All cell assembly and disassembly operations were performed in an Ar-filled dry glovebox (oxygen level <2 ppm).

**Synchrotron XRF Microscopy.** XRF was performed at the 2-ID-D beamline at the Advanced Photon Source (APS) at Argonne National Laboratories, where an undulator source was used to create hard X-rays with energies of 1.75−10 keV and focused using Fresnel zone plate optics. Emitted X-ray fluorescence was detected using an energy-dispersive germanium detector (LEGe detector, Canberra).

**Synchrotron SAXS/WAXS Measurements.** SAXS/WAXS data were collected at Beamline 12ID-B of the APS at the Argonne National Laboratory. The X-ray was focused, and the spot size on the sample was ~50 $\mu$m × 50 $\mu$m. SAXS and WAXS data were presented in momentum transfer, $q$ ($q = 4\pi \sin\theta/\lambda$, where $\theta$ is one-half of the scattering angle, and $\lambda$ = 1.033 Å is the wavelength of the 12 keV energy probing X-ray), measured in the range 0.01−2.3 $Å^{-1}$. The charged samples were prepared by stripping $V_2O_5$ films onto Kapton tape. The discharged samples were scratched off and sealed inside a 3 mm diameter hole in a piece of aluminum foil by sealing the Kapton sheet to the foil using epoxy. All cell assembly and disassembly operations were performed in a He-filled dry glovebox (oxygen level <2 ppm).

**XPS.** A Scienta hemispherical electron analyzer (SES100) was used to obtain the XPS/UPS measurements, and total energy resolution of the spectra, including photon energy, was set to less than ~0.1 eV. The acceptance angle for incoming electrons is 5 degrees. All experimental data were taken under a pressure of $2 \times 10^{-10}$ Torr or less.

**Electron Microscopy.** Scanning electron microscopy (SEM) images were recorded with a JEOL JSM-7500F field emission SEM operating at 30 kV. HRTEM images were recorded on a JEOL EM-2100F. HAADF images and line scans were obtained using JEM-ARM200CF, a probe aberration-corrected 200 kV STEM/TEM with a cold field emission source with a 0.35 eV energy resolution.

**XANES.** X-ray spectroscopy and extended X-ray absorption fine structure (EXAFS) measurements were performed at PNC-XOR bending magnet beamline (20-BM-B) of APS in Argonne National Laboratory. Measurements at the V K-edge were performed under transmission mode using gas ionization chambers to monitor the incident and transmitted X-ray intensities. A third ionization chamber was used in conjunction with a Ti-foil standard to provide internal calibration for the alignment of the edge positions. The incident beam was monochromatized using a Si (111) double crystal fixed exit monochromator. Harmonic rejection was accomplished using a rhodium-coated mirror. The charged samples were prepared by stripping $V_2O_5$ films onto Kapton tape. The discharged samples were scratched off and sealed inside a 3 mm diameter hole in a piece of aluminum foil by sealing the Kapton sheet to the foil using epoxy. All cell assembly and disassembly operations were performed in a He-filled dry glovebox (oxygen level <2 ppm). The reference standards ($V^{5+}$ and $V^{4+}$) were prepared by spreading thin, uniform layers of the $V_2O_5$ and $VO_2$ powder on Kapton tape and stacking a few layers to attain the desired absorption step height. Each spectrum was normalized using the data processing software package IFEFFIT.[37] The alignment of each sample reference spectrum with respect to the V standard spectrum is within the range ±0.03 eV.

**MD Simulations.** The atomistic model of $V_2O_5$ layers was prepared in reference to crystallographic data.[38] Bonding parameters of the $V_2O_5$ layers were assigned based on the same data, while van der Waals parameters were adopted from other studies.[39] Partial charges of the $V_2O_5$ layers were assigned to their oxidation states. The TIP3P model was used to describe the water molecules. The CHARMM force field[40] was used for the parameters of Mg ions and water molecules. Molecular dynamics simulations were performed using NAMD[41,42] with a simulation time step of 2 fs. The simulations were run under an isothermal−isobaric (NPT) ensemble at a temperature of $T$ = 300 K, using a Langevin damping constant of $\gamma_{Lang} = 0.01$ $ps^{-1}$. Periodic boundary conditions were applied to the system, and the particle Ewarld summation algorithm[43] was used to compute long-range electrostatics.

*Conflict of Interest:* The authors declare no competing financial interest.

*Supporting Information Available:* XRF imaging analysis for self-absorption of Mg in $VO_2/V_2O_5$ is presented. Synchrotron X-ray diffraction of a bilayered vanadium cathode in the charged and discharged state in conjunction with large-area EDAX analysis is also shown. The Supporting Information is available free of charge on the ACS Publications website at DOI: 10.1021/acsnano.5b02450.

*Acknowledgment.* This work was performed, in part, at the Center for Nanoscale Materials, a U.S. Department of Energy Office of Science User Facility under Contract No. DE-AC02-06CH11357. Use of the Advanced Photon Source, an Office of Science User Facility, was supported by the U.S. Department of Energy, Office of Science, Office of Basic Energy Sciences, under contract no. DE-AC02-06CH11357. The work at the Joint Center for Energy Storage Research (JCESR), an Energy Innovation Hub, was funded by the Department of Energy, Office of Science, Basic Energy Sciences, is operated under Contract No. DE-AC02-06CH11357. The authors would like to thank Pietro P. Lopes for assistance with FTIR measurements. S.T. prepared all samples and performed their characterization. D.Z. prepared the high-energy ball-milled Sn anode and performed long cycling of the full Mg cells. Y.L. performed HRTEM as well as HAADF measurements. B.L. and J.M. performed XRF imaging measurements. H.C. and P.K. performed MD simulations, and V.S., N.M., C.J., and T.R. directed the research and performed data analysis.

## REFERENCES AND NOTES

1. Armand, M.; Tarascon, J. M. Building Better Batteries. *Nature* **2008**, *451*, 652.
2. Novak, P.; Imhof, R.; Haas, O. Magnesium Insertion Electrodes for Rechargeable Nonaqueous Batteries - A Competitive Alternative to Lithium?. *Electrochim. Acta* **1999**, *45*, 351.
3. Lu, Z.; Schechter, A.; Moshkovich, M.; Aurbach, D. On the Electrochemical Behavior of Magnesium Electrodes in Polar Aprotic Electrolyte Solutions. *J. Electroanal. Chem.* **1999**, *466*, 203.
4. Levi, E.; Gofer, Y.; Aurbach, D. On the Way to Rechargeable Mg Batteries: The Challenge of New Cathode Materials. *Chem. Mater.* **2010**, *22*, 860.
5. Muldoon, J.; Bucur, C. B.; Oliver, A. G.; Sugimoto, T.; Matsui, M.; Kim, H. S.; Allred, G. D.; Zajicek, J.; Kotani, Y. Electrolyte Roadblocks to a Magnesium Rechargeable Battery. *Energy Environ. Sci.* **2012**, *5*, 5941.
6. Aurbach, D.; Lu, Z.; Schechter, A.; Gofer, Y.; Gizbar, H.; Turgeman, R.; Cohen, Y.; Moshkovich, M.; Levi, E. Prototype

Systems for Rechargeable Magnesium Batteries. *Nature* **2000**, *407*, 724.
7. Aurbach, D.; Schechter, A.; Moshkovich, M.; Cohen, Y. On the Mechanisms of Reversible Magnesium Deposition Processes. *J. Electrochem. Soc.* **2001**, *148*, A1004.
8. Mizrahi, O.; Amir, N.; Pollak, E.; Chusid, O.; Marks, V.; Gottlieb, H.; Larush, L.; Zinigrad, E.; Aurbach, D. Electrolyte Solutions with a Wide Electrochemical Window for Recharge Magnesium Batteries. *J. Electrochem. Soc.* **2008**, *155*, A103.
9. Yoshimoto, N.; Yakushiji, S.; Ishikawa, M.; Morita, M. Rechargeable Magnesium Batteries with Polymeric Gel Electrolytes Containing Magnesium Salts. *Electrochim. Acta* **2003**, *48*, 2317.
10. Yoo, H. D.; Shterenberg, I.; Gofer, Y.; Gershinsky, G.; Pour, N.; Aurbach, D. Mg Rechargeable Batteries: An On-Going Challenge. *Energy Environ. Sci.* **2013**, *6*, 2265.
11. Tao, Z. L.; Xu, L. N.; Gou, X. L.; Chen, J.; Yuan, H. T. $TiS_2$ Nanotubes as the cathode materials of mg-ion batteries. *Chem. Commun.* **2004**, 2080.
12. Liang, Y. L.; Feng, R. J.; Yang, S. Q.; Ma, H.; Liang, J.; Chen, J. Rechargeable mg Batteries with Graphene-Like $MoS_2$ Cathode and Ultrasmall Mg Nanoparticle Anode. *Adv. Mater.* **2011**, *23*, 640.
13. Nuli, Y. N.; Zheng, Y. P.; Wang, F.; Yang, J.; Minett, A. I.; Wang, J. L.; Chen, J. MWNT/c/$Mg_{1.03}Mn_{0.97}SiO_4$ Hierarchical Nanostructure for Superior Reversible Magnesium Ion Storage. *Electrochem. Commun.* **2011**, *13*, 1143.
14. Livage, J. Hydrothermal Synthesis of Nanostructured Vanadium Oxides. *Materials* **2010**, *3*, 4175.
15. Imamura, D.; Miyayama, M. Characterization of Magnesium-Intercalated $V_2O_5$/Carbon Composites. *Solid State Ionics* **2003**, *161*, 173.
16. Gershinsky, G.; Yoo, H. D.; Gofer, Y.; Aurbach, D. Electrochemical and Spectroscopic Analysis of $Mg^{2+}$ Intercalation into Thin Film Electrodes of Layered Oxides: $V_2O_5$ and $MoO_3$. *Langmuir* **2013**, *29*, 10964.
17. Kim, R. H.; Kim, J. S.; Kim, H. J.; Chang, W. S.; Han, D. W.; Lee, S. S.; Doo, S. G. Highly Reduced VOx Nanotube Cathode Materials with Ultra-High Capacity for Magnesium Ion Batteries. *J. Mater. Chem. A* **2014**, *2*, 20636.
18. Lee, S. H.; DiLeo, R. A.; Marschilok, A. C.; Takeuchi, K. J.; Takeuchi, E. S. Sol Gel Based Synthesis and Electrochemistry of Magnesium Vanadium Oxide: A Promising Cathode Material for Secondary Magnesium Ion Batteries. *ECS Electrochem. Lett.* **2014**, *3*, 87.
19. Tepavcevic, S.; Xiong, H.; Stamenkovic, V. R.; Zuo, X. B.; Balasubramanian, M.; Prakapenka, V. B.; Johnson, C. S.; Rajh, T. Nanostructured Bilayered Vanadium Oxide Electrodes for Rechargeable Sodium-Ion Batteries. *ACS Nano* **2012**, *6*, 530.
20. Atkins, P.; De Paola, J. *Physical Chemistry*; W.H. Freeman and Company: New York, 2006.
21. Giorgetti, M.; Berrettoni, M.; Smyrl, W. H. Doped $V_2O_5$-Based Cathode Materials: Where Does the Doping Metal Go? An X-Ray Absorption Spectroscopy Study. *Chem. Mater.* **2007**, *19*, 5991.
22. Malucelli, E.; Iotti, S.; Fratini, M.; Marraccini, C.; Notargiacomo, A.; Gianoncelli, A.; Bukreeva, I.; Cedola, A.; Maier, J.; Farruggia, G.; *et al.* X-ray Fluorescence Microscopy of Light Elements in Cells: Self-Absorption Correction by Integration of Compositional and Morphological Measurements, *11th International Conference on X-Ray Microscopy (Xrm2012)*; **2013**, Vol. *463*.012022
23. Seng, K. H.; Liu, J.; Guo, Z. P.; Chen, Z. X.; Jia, D.; Liu, H. K. Free-Standing $V_2O_5$ Electrode for Flexible Lithium Ion Batteries. *Electrochem. Commun.* **2011**, *13*, 383.
24. Novak, P.; Desilvestro, J. Electrochemical Insertion of Magnesium in Metal-Oxides and Sulfides from Aprotic Electrolytes. *J. Electrochem. Soc.* **1993**, *140*, 140.
25. Novak, P.; Scheifele, W.; Joho, F.; Haas, O. Electrochemical Insertion of Magnesium into Hydrated Vanadium Bronzes. *J. Electrochem. Soc.* **1995**, *142*, 2544.
26. Subbaraman, R.; Tripkovic, D.; Chang, K.-C.; Strmcnik, D.; Paulikas, A. P.; Hirunsit, P.; Chan, M.; Greeley, J.; Stamenkovic, V.; Markovic, N. M. Trends in Activity for the Water Electrolyser Reactions on 3d M(Ni,Co,Fe,Mn) Hydr(Oxy)Oxide Catalysts. *Nat. Mater.* **2012**, *11*, 550.
27. Wang, Y.; Shang, H. M.; Chou, T.; Cao, G. Z. Effects of Thermal Annealing on the $Li^+$ Intercalation Properties of $V_2O_5$ $nH_2O$ Xerogel Films. *J. Phys. Chem. B* **2005**, *109*, 11361.
28. Pajchel, L.; Kolodziejski, W. Solid-State MAS, NMR, TEM, and TGA Studies of Structural Hydroxyl Groups and Water in Nanocrystalline Apatites Prepared by Dry Milling. *J. Nanopart. Res.* **2013**, *15*, 10.1007/s11051-013-1868-y.
29. Petkov, V.; Trikalitis, P. N.; Bozin, E. S.; Billinge, S. J. L.; Vogt, T.; Kanatzidis, M. G. Structure of $V_2O_5$ $nH_2O$ Xerogel Solved By The Atomic Pair Distribution Function Technique. *J. Am. Chem. Soc.* **2002**, *124*, 10157.
30. Cha, J. N.; Cheong, B. S.; Cho, H. G. Solvation of $Mg(ClO_4)_2$ in Deuterated Acetonitrile Studied by Means of Vibrational Spectroscopy. *J. Phys. Chem. A* **2001**, *105*, 1789.
31. Pavlov, M.; Siegbahn, P. E. M.; Sandstrom, M. Hydration of Beryllium, Magnesium, Calcium, and Zinc Ions Using Density Functional Theory. *J. Phys. Chem. A* **1998**, *102*, 219.
32. Jiao, D.; King, C.; Grossfield, A.; Darden, T. A.; Ren, P. Simulation of $Ca^{2+}$ and $Mg^{2+}$ solvation Using Polarizable Atomic Multipole Potential. *J. Phys. Chem. B* **2006**, *110*, 18553.
33. Fu, J. W.; Yang, Y. S. Formation of the Solidified Microstructure In Mg-Sn Binary Alloy. *J. Cryst. Growth* **2011**, *322*, 84.
34. Saatci, B.; Ari, M.; Gunduz, M.; Turktekin, S.; Meydaneri, F.; Durmus, S.; Ozdemir, M. Structural and Transport Properties of Sn-Mg Alloys. *Continuum Mech. Thermodyn.* **2013**, *25*, 739.
35. Singh, R. N.; Jha, I. S.; Pandey, D. K. Thermodynamics of Liquid Mg-Sn Alloys. *J. Phys.: Condens. Matter* **1993**, *5*, 2469.
36. Singh, N.; Arthur, T. S.; Ling, C.; Matsui, M.; Mizuno, F. A High Energy-Density Tin Anode for Rechargeable Magnesium-Ion Batteries. *Chem. Commun.* **2013**, *49*, 149.
37. Newville, M. Ifeffit: Interactive XAFS Analysis and FEFF Fitting. *J. Synchrotron Radiat.* **2001**, *8*, 322.
38. Wyckoff, R. *The Structure of Crystals*; The Chemical Catalog Company, Inc.: New York, 1924.
39. Cundari, T. R.; Saunders, L.; Sisterhen, L. L. Molecular Modeling of Vanadium-Oxo Complexes. A Comparison of Quantum and Classical Methods. *J. Phys. Chem. A* **1998**, *102*, 997.
40. MacKerell, A. D.; Bashford, D.; Bellott, M.; Dunbrack, R. L.; Evanseck, J. D.; Field, M. J.; Fischer, S.; Gao, J.; Guo, H.; Ha, S.; *et al.* All-Atom Empirical Potential for Molecular Modeling and Dynamics Studies of Proteins. *J. Phys. Chem. B* **1998**, *102*, 3586.
41. Phillips, J. C.; Braun, R.; Wang, W.; Gumbart, J.; Tajkhorshid, E.; Villa, E.; Chipot, C.; Skeel, R. D.; Kale, L.; Schulten, K. Scalable Molecular Dynamics With NAMD. *J. Comput. Chem.* **2005**, *26*, 1781.
42. Humphrey, W.; Dalke, A.; Schulten, K. VMD: Visual Molecular Dynamics. *J. Mol. Graphics* **1996**, *14*, 33.
43. Darden, T.; York, D.; Pedersen, L. Particle Mesh Ewald - an N. Log(N) Method for Ewald Sums in Large Systems. *J. Chem. Phys.* **1993**, *98*, 10089.